THE SENSITIVITY OF TURBINE CASCADE ENDWALL LOSS TO INLET BOUNDARY LAYER THICKNESS

ABSTRACT

The development of hub and casing boundary layers through a turbomachine is difficult to predict, giving rise to uncertainty in the boundary conditions experienced by each blade row. Previous studies in turbine cascades disagree on the sensitivity of endwall loss to such inlet conditions. This paper explores the problem computationally, by examining a large number of turbine cascades and varying the inlet boundary layer thickness.

It is demonstrated that the sensitivity of endwall loss to inlet conditions is design dependent, and determined by the component of endwall loss associated with the secondary flow. This Secondary-Flow-Induced loss is characterised by a vorticity factor based on classical secondary flow theory. Designs that produce high levels of secondary vorticity tend to generate more loss and are more sensitive to inlet conditions. This sensitivity is largely driven by the dissipation of Secondary Kinetic Energy (SKE): thickening the inlet boundary layer causes the secondary vorticity at the cascade exit to be more dispersed within the passage, resulting in larger secondary flow structures with higher SKE. The effects are captured using a simple streamfunction model based on classical secondary flow theory, which has potential for preliminary design and sensitivity assessment.

1. INTRODUCTION

Endwall losses are generated by dissipation in the endwall boundary layers and mixing processes. In particular, significant mixing loss may be produced by the secondary flows, which are generated as the non-uniform inlet flow is turned through the blade row.

Of the many aerodynamic and design factors that can influence endwall loss in turbomachinery flows, this paper focuses on the impact of inlet conditions. This sensitivity is of practical importance since the actual boundary conditions inside a machine are unlikely to be known accurately, therefore robust design strategies must be adopted.

This study considers linear cascades with steady inflow, which represent a constrained sub-section of the turbine design space. Nonetheless cascades reproduce many of the underlying physical effects observed in annular turbines and have furthered understanding of the basic problem, as illustrated by the reviews of Sieverding [1] and Langston [2]. Most experimental cascades operate with an inlet endwall boundary layer formed naturally on the internal upstream walls of the wind-tunnel. Multi-stage inlet flows are more complex due to secondary flows convecting from upstream blade rows and endwall boundary layer skew, and this can lead to additional losses (e.g. Denton and Pullan [6]). This paper does not examine these effects, rather it attempts to understand the sensitivity of endwall loss to inlet boundary layer thickness for a simple, collinear turbulent profile.

Several authors have examined the effects of inlet boundary layer thickness on cascade loss by installing steps or bleed slots upstream of the test section. Reviewing data from several cascades, Sharma and Butler [8] argued that the *net* mass-averaged endwall loss is approximately independent of the inlet boundary layer thickness. Similar observations have been made by other authors (e.g. Hodson & Dominy [10]), but there are some notable exceptions. For example, de la Rosa Blanco et al. [11] examined two low pressure turbine blades with identical flow angles but different blade thickness. Increasing the size of the turbulent inlet boundary layer, they found that the endwall loss increased for both blades but more rapidly for the thinner blade. This results illustrates a key finding of the current study, namely that the impact of inlet conditions on endwall loss depends on the design of the blade itself.

The following section describes a computational study of parametric cascade designs. Subsequent sections discuss the impact of inlet boundary layer thickness on endwall loss, the loss mechanisms that drive the sensitivity, and the ability of classical secondary flow theory to model the sensitivity observed.

		Range
	Inlet Flow Angle α_1	-20°→ 40°
	Outlet Flow Angle α_2	-50°→ -70°
	Flow Turning	30°→ 110°
	Zweifel Coefficient	0.51 → 1.26
	Midspan Exit Mach number M_2	0.7
	Reynolds number Re_{C_x}	200,000
	Aspect Ratio H/C_x	3
	Inlet momentum thickness θ/C_x	0.002 → 0.05
Suction Side C_p	Diffusion Factor DF	0.16 → 0.40
	Peak Suction Location PSL	0.42 → 0.62
Thickness	Max. Thick. T_{max}/C_x	0.15 → 0.20
	Max. Thick. Location (x/C_x)	0.35
	TE Thickness t/C_x	0.02
	TE wedge angle	6° → 9°

Table 1 : Cascade Design Parameters.

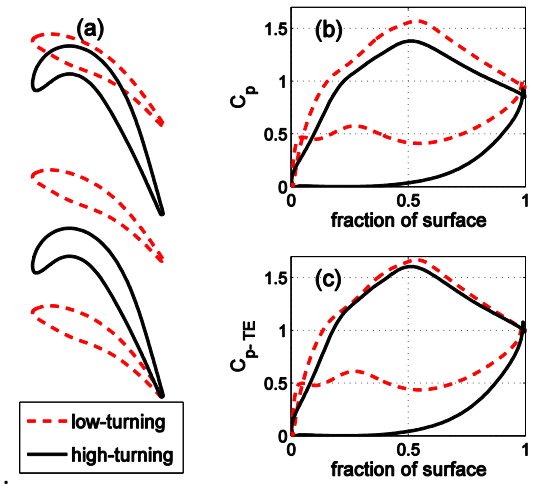

Figure 1 Low-turning and high-turning profiles (a) and midspan pressure distributions (b,c) (CFD, $\theta/C_x = 0.01$).

2. NUMERICAL METHODS

2.1 Cascade Designs

The cascade geometries considered in this paper are taken from the parametric study of Coull [3]. As summarised in Table 1, these 150+ designs cover a large range of flow angles and blade thickness, with different suction surface loading styles (diffusion factor and peak suction location). The previous study considered a constant inlet boundary layer thickness ($\theta/C_x = 0.01$). In this paper, the thickness of the turbulent boundary layer at the inlet is varied from $\theta/C_x = 0.002 \rightarrow 0.05$ for a selected number of these designs, at an aspect ratio of $H/C_x = 3$.

For illustrative purposes, the behaviour of two designs will be described in detail: a low-turning design ($\alpha_1 = -20°$, $\alpha_2 = -50°$) and a high-turning design ($\alpha_1 = 40°$, $\alpha_2 = -70°$), which approximately represent the extremes of minimum and maximum endwall loss respectively. The geometry and pressure distributions are shown in Figure 1. It can be seen that the suction side C_p distributions are similar for the two designs, in particular when they are normalised by the local value at the trailing edge (Figure 1(c)). There is a marked difference in the level of pressure side loading, with the low-turning design having much higher velocity. This effect is a consequence of the cross-passage pressure gradient in the covered turning region, which is largely determined by the flow angles [3]. The two designs have matching thickness distributions, with a maximum thickness of $0.2C_x$ at an axial location of $x/C_x = 0.35$, a trailing edge thickness of $0.02C_x$ and a trailing edge wedge angle of 9°.

2.2 Meshing and CFD

Automated meshing is performed using an optimiser [3] built around the Rolls-Royce PADRAM code [12], which combines a blade O-mesh with multi-block passage H-meshes. A maximum y^+ value of approximately unity is achieved on the blade and endwall surfaces, with an expansion ratio of 1.14. The final meshes have around 10 million cells for each case. Further refinements in the mesh caused changes in passage, profile and endwall loss coefficients of less than 0.00005.

Steady RANS calculations are performed with the Rolls-Royce in-house solver HYDRA. The spatial discretization is based on an upwind edge-based finite volume scheme and is second-order accurate ([13]). Calculations are performed using the two-equation Shear-Stress-Transport turbulence model, with fully-turbulent boundary layers. A half-passage domain is used for each cascade, with an inviscid wall at midspan to provide symmetry. The inlet is located at a distance of $0.8C_x$ upstream of the leading edge and the domain outlet is $1.2C_x$ downstream of the trailing edge. To calculate loss coefficients, flow parameters are extracted at an "outlet" plane located at an axial distance of $0.5C_x$ downstream of the trailing edge. Spanwise distributions of total pressure, total temperature, flow angles and turbulence parameters are specified at the inlet, and static pressure at the exit. A collinear turbulent boundary layer is specified at the inlet by scaling total pressure and turbulence statistics from a separate flat-plate boundary layer calculation. The freestream flow turbulence parameters are set to obtain a turbulence level of 5% with an integral length scale of $0.1C_x$, which is broadly representative of a multistage turbine [14].

To assess the accuracy of the CFD, calculations are performed for experimental cascade studies ([9], [10] [11]). Figure 2 compares measured and calculated endwall total pressure loss coefficients; the average error is less than 10%, which is deemed to be acceptable.

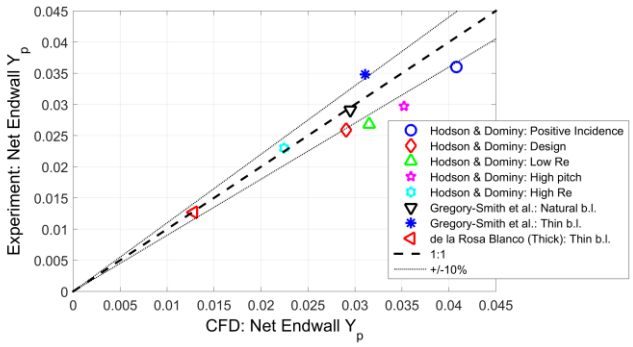

Figure 2 Experimental Validation ([9], [10], [11]).

2.3 Loss Coefficients

This paper considers entropy loss coefficients which give a measure of lost work [5]. The general expression for entropy loss coefficient is:

$$\xi = \frac{(s_2 - s_{inlet-REF})}{[(h_{02} - h_2)/T_2]_{outlet-REF}} \qquad (1)$$

where s is the specific entropy, h is the specific enthalpy and T is the static temperature. This paper considers the mixed-out entropy at the outlet plane ($s_2 = s_{2,mix}$). To obtain a net passage loss coefficient, the inlet reference entropy $s_{inlet-REF}$ may be taken as the mass-averaged value, or a mixed-out condition. For a thin inlet boundary layer there is little difference between these definitions but the choice is more significant for thicker inlet boundary layers. Analysis of the trends in the current study suggests that it is most appropriate to use the inlet mass-averaged entropy $\overline{s_1}$ in equation (1); this reflects the physical reality that the inlet boundary layer fluid does not undergo significant mixing before entering the blade row.

The term $[(h_{02} - h_2)/T_2]_{outlet-REF}$ in equation (1) can be considered as a reference dynamic entropy. For the net passage loss, this reference is calculated using the mass-averaged inlet condition and the area-averaged outlet pressure ($P_2 \approx$ constant), such that:

$$\xi_{net} = \frac{(s_{2,mix} - \overline{s_1})}{[(h_{02} - h_2)/T_2]_{isen}} \approx \frac{(s_{2,mix} - \overline{s_1})}{c_p\left(\left(\frac{\overline{P_{01}}}{P_2}\right)^{(\gamma-1)/\gamma} - 1\right)} \qquad (2)$$

The two-dimensional profile loss is calculated using only the midspan conditions for the inlet and dynamic references:

$$\xi_{mid} \approx \frac{(s_{2,mid,mix} - s_{1,mid})}{c_p\left(\left(\frac{P_{01,mid}}{P_2}\right)^{(\gamma-1)/\gamma} - 1\right)} \qquad (3)$$

The endwall loss coefficient ξ_{end} is then given by:

$$\xi_{end} = \xi_{net} - \xi_{mid} \qquad (4)$$

The passage and profile loss coefficients in equations (2) and (3) have subtly different denominators, which allows for the fact that the two-dimensional losses at each spanwise height will scale with the *local dynamic conditions*. In the limit of extremely thick inlet boundary layers, significant portions of the blade span will have lower freestream velocity than the midspan and will therefore generate less entropy. Integrated up the span, the profile loss contribution therefore scales with the mass-averaged dynamic conditions, which is accounted for by the switch of dynamic reference between equations (2) and (3).

3. ENDWALL LOSS SENSITIVITY

3.1 Vorticity Amplification Factor

In order to quantify the secondary flow characteristics of different cascades, Coull [3] defined a vorticity "Amplification Factor" using the classical theory of Marsh [4]. This parameter is a measure of *the area-average secondary vorticity* $\overline{\omega_{sec}}$ at the exit of each turbine cascade:

$$AF_{Marsh} = 2M^*\left(\frac{V_1}{V_2}\right)^2\left[\frac{\Delta T^* C_x}{p\cos\alpha_2} + \frac{\left|\frac{V_2}{V_1}\sin\alpha_1 - \sin\alpha_2\right|}{\cos\alpha_2}\right] \qquad (5)$$

where p is the pitch, M^* is a compressibility factor (≈1) and ΔT^* is the non-dimensional difference in transit time between flow passing over the pressure and suction surfaces:

$$M^* = \left(1 + \frac{\gamma - 1}{2} M_1^2\right) \quad (6)$$

$$\Delta T^* = T_{PS}^* - T_{SS}^* = \oint \left(\frac{V_2}{V_{fs}}\right) d\left(\frac{S}{C_x}\right) \quad (7)$$

The integral in equation (7) is performed over the blade in a similar manner to circulation. The Amplification Factor AF_{Marsh} is highly sensitive to flow angles and pressure surface velocity, being around 0.7 for the low-turning design in Figure 1 and 7.7 for the high-turning design.

Figure 3 shows the relationship between AF_{Marsh} and endwall loss for around 150 turbine cascades. The inlet boundary layer thickness has been varied for several individual designs, indicated by the solid lines. In general, designs with higher Amplification Factor have higher endwall losses, and greater sensitivity to the inlet conditions.

3.2 Background Dissipation and Secondary-Flow-Induced-Loss

A portion of the endwall loss in Figure 3 is generated by viscous shear in the boundary layers on the endwall surface (inside the blade passage and on the platforms upstream and downstream of the blade row). This component of loss is quantified by calculating the "Background Dissipation" loss, ξ_{CD}, which represents the viscous losses associated with the *wetted area of the endwall, independent of the secondary flow*. As discussed by Denton [5], the rate of entropy generation in a boundary layer (per unit surface area) is approximately proportional to the cube of velocity. For each CFD solution, the local freestream Mach number over the endwall is estimated from the calculated static pressures and the inlet freestream quantities [3]. An estimate of the specific entropy rise Δs_{CD} is then obtained by integration over the endwall surface:

$$\Delta s_{CD} = \frac{1}{\dot{m}} \int_{inlet}^{outlet} C_D \frac{\rho_{fs} V_{fs}^3}{T_{fs}} dA_{end} \quad (8)$$

The Dissipation Coefficient C_D is assumed to equal 0.002, which Denton [5] argued is a reasonable approximation. The Background Dissipation loss coefficient is then given by:

$$\xi_{CD} = \frac{\Delta s_{CD}}{C_p \left(\left(\frac{\overline{P_{01}}}{P_2}\right)^{(\gamma-1)/\gamma} - 1\right)} \quad (9)$$

Provided the assumption of constant C_D is reasonable, the Background Dissipation loss is effectively independent of the inlet boundary layer thickness.

The remaining component of endwall loss is generated by the secondary flows and associated mixing processes:

$$\xi_{sec-flow} = \xi_{end} - \xi_{CD} \quad (10)$$

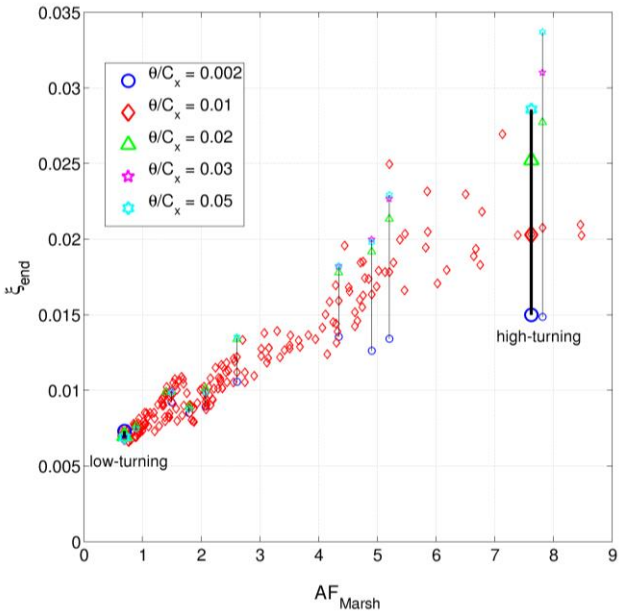

Figure 3: Endwall Loss vs. Vorticity Amplification Factor (eq. (5)), with varying inlet boundary layer thickness.

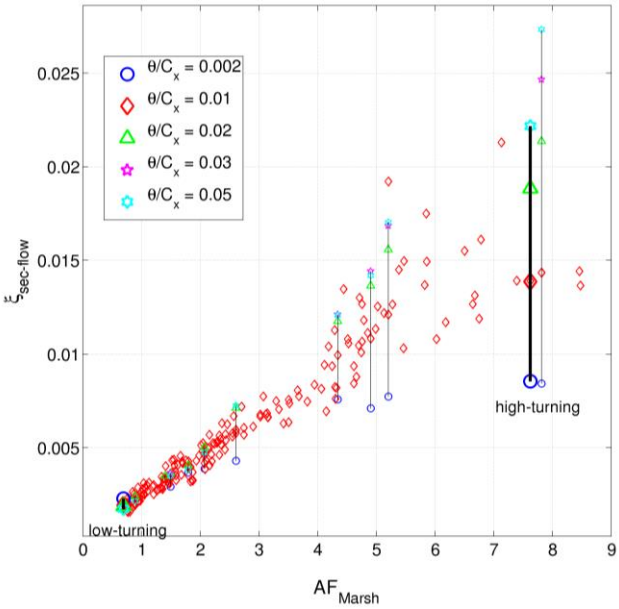

Figure 4: Secondary-flow-induced-loss (eq. (10)) vs. Vorticity Amplification Factor (eq. (5)), for varying inlet boundary layer thickness.

This definition includes the losses associated with the mixing-out of the non-uniform inlet flow, in addition to those directly associated with the secondary flow; in practice it is difficult to separate these effects.

Figure 4 plots the Secondary-Flow-Induced Loss $\xi_{sec-flow}$ against the Amplification Factor AF_{Marsh} in a similar manner to Figure 3. For a constant inlet boundary layer thickness of $\theta/C_x = 0.01$ (red diamonds), there is an approximately proportional trend between $\xi_{sec-flow}$ and AF_{Marsh}. This behaviour was observed in the previous study [3]. For several individual designs the inlet boundary layer thickness has been varied. For designs with low AF_{Marsh} there is no discernible sensitivity to the inlet condition. In contrast, designs with high AF_{Marsh} show significant variation: for the high-turning design, $\xi_{sec-flow}$ increases by around 175% between the thinnest and thickest boundary layers studied.

3.3 Previous Experimental Results

The current results shed some light onto the apparent contradictions in the literature regarding sensitivity to inlet conditions. Figure 5 presents net endwall losses against Amplification Factor (equation (5)) for four cascade designs where the geometry was available. The endwall losses have been re-scaled to match the aspect ratio used in the current study ($h/C_x = 3$). There are notable differences in the ranges of inlet boundary layer thickness studied, extent of the exit domain traversed and the definitions of loss coefficient used by each author. Nonetheless, the experimental results fall within the scatter of calculated endwall losses observed in Figure 3. Again, the designs with large Amplification Factors tend to have higher loss and greater sensitivity to inlet conditions.

One may conclude that the sensitivity to inlet conditions is driven by the secondary flow, which can be characterised by the Amplification Factor. The remainder of this paper seeks to understand the physical mechanisms that determine this sensitivity in more detail.

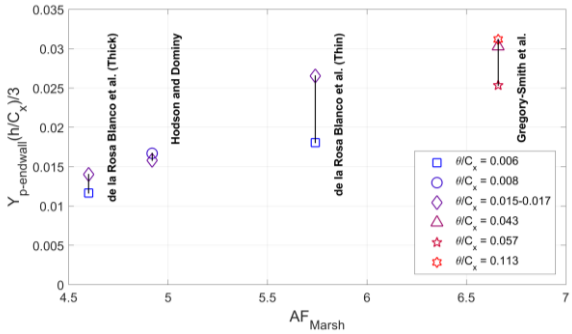

Figure 5: Endwall loss vs. Amplification Factor for experimental cases with turbulent inlet boundary layers ([9], [10], [11]).

4. SECONDARY-FLOW-INDUCED LOSS MECHANISMS

This section discusses the three key loss mechanisms that compose the Secondary-Flow-Induced loss ($\xi_{sec-flow}$):

1) The interaction of secondary flows with blade surface boundary layers;
2) The dissipation of Secondary Kinetic Energy (SKE);
3) The mixing-out of Streamwise Momentum Deficits, e.g. regions of low total pressure.

Directly separating the above mechanisms is challenging, even in a CFD calculation. Instead their role is inferred by examining the flow field at the trailing edge plane ($x/C_x = 1$) for each cascade, and then considering the losses inside the passage and the downstream mixing process.

4.1 Losses Inside the Passage

Some of the loss generated by the secondary flow occurs upstream of the trailing edge plane, including interaction with blade surface boundary layers (1, above), and partial mixing-out of SKE (2) and Streamwise Momentum Deficits (3). The resultant in-passage loss has been quantified by calculating the mass-averaged secondary-flow-induced loss at the trailing edge plane:

$$\xi_{sec-flow-TE} = [\xi_{end} - \xi_{CD}]_{TE,mass-ave} \qquad (11)$$

Here ξ_{CD} is calculated by performing the integral in equation (8) up to the trailing edge plane. The in-passage loss is plotted against the Amplification Factor (equation (5)) in Figure 6. Individual designs have been indicated by the solid lines. Noting the overall levels of secondary-flow-induced loss in Figure 4, it can be seen that the in-passage losses represent only a small fraction of the total, being close to zero for $AF_{Marsh} < 2$. For the high-turning design the in-passage loss rises to up to 0.4%. Analysis of the streamwise development of losses ([15]) suggests that this effect is largely driven by the partial mixing-out of Secondary Kinetic Energy within the passage. One may therefore conclude that the interaction of secondary flows with blade surface boundary layers does not contribute significantly to endwall loss in cascades. The mixing-out of streamwise momentum deficits inside the passage is also believed to be small.

4.2 Secondary Kinetic Energy (SKE)

The secondary velocities are by definition normal to the primary flow direction, which is determined by the midspan flow angle at each pitchwise location, as for example defined by [6]. The importance of this definition will be demonstrated in section 5.2 below. The losses associated with the mixing-out of SKE downstream of the trailing edge have been estimated by considering *localised*, constant-pressure mixing. If the secondary velocity is dissipated, the total pressure will drop such that:

$$\frac{\Delta P_0}{P} = \left(1 + \frac{\gamma - 1}{2} M_{total}^2\right)^{\frac{\gamma}{\gamma-1}} - \left(1 + \frac{\gamma - 1}{2} M_{stream}^2\right)^{\frac{\gamma}{\gamma-1}} \qquad (12)$$

where M_{total} is the magnitude of the local Mach number, M_{stream} is the streamwise component, γ is the ratio of specific heat capacities and P is the local static pressure. The corresponding increase in specific entropy Δs_{SKE} is given by:

$$\Delta s_{SKE} = R \ln\left(\frac{P_0}{P_0 - \Delta P_0}\right) \qquad (13)$$

where R is the gas constant. An SKE loss coefficient is then calculated using the mass-averaged entropy increase $\overline{\Delta s_{SKE}}$:

$$\xi_{SKE} = \frac{\overline{\Delta s_{SKE}}}{c_p\left(\left(\frac{\overline{P_{01}}}{P_2}\right)^{(\gamma-1)/\gamma} - 1\right)} \qquad (14)$$

This definition does not include any mixing-out between adjacent fluid particles and only includes the loss that is directly associated with the SKE.

The resultant SKE losses have been presented against the Amplification Factor in Figure 7. For low-AF_{Marsh} designs, the SKE losses are near-zero and increases in the inlet boundary layer thickness result in only small (absolute) increases in loss. In contrast, for high-turning designs the SKE is large and highly sensitive to the inlet conditions. Comparison with Figure 4 shows that the changes in ξ_{SKE} are almost wholly responsible for the overall sensitivity to inlet conditions for each design. As will be discussed in section 5.2, the trends in Figure 7 are driven by:

1) Changes in the average streamwise vorticity, as captured by the Amplification Factor AF_{Marsh};
2) The distribution of that vorticity within the passage, largely a function of the inlet boundary layer thickness.

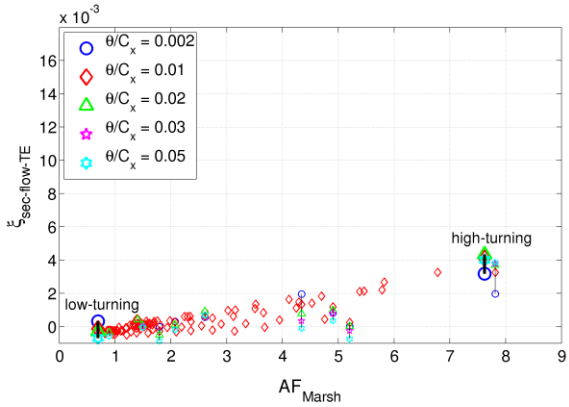

Figure 6: In-Passage Secondary-Flow-Induced Loss.

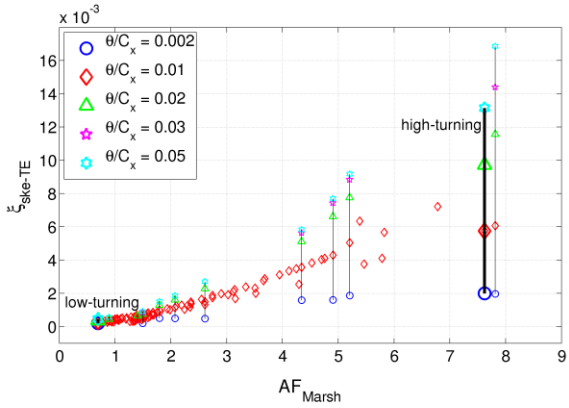

Figure 7: Loss due to the mixing-out of SKE downstream of the TE.

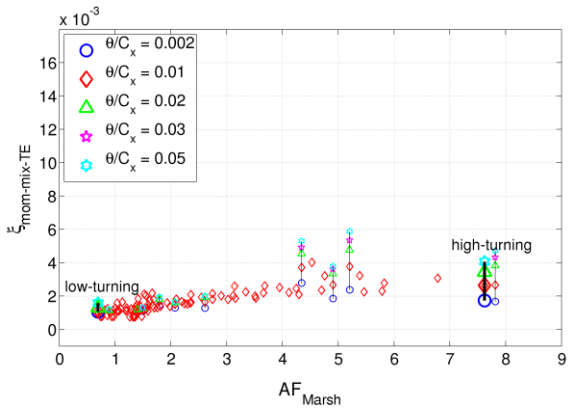

Figure 8: Loss due to the mixing-out of streamwise momentum deficits downstream of the TE.

4.3 Streamwise Momentum Deficits

The final component of mixing loss occurs due to the mixing of unlike streams ([5]). Considering a control volume downstream of the trailing edge, this mixing loss is driven by the *streamwise momentum deficits* of the flow leaving the cascade. Such deficits arise due to the convection and distortion of the (low-total-pressure) inlet boundary layer fluid, the development of losses in the passage, and from regions of significant under- and over-turning induced by the secondary flow.

From the trailing edge data, a constant-area mixing calculation is performed and the endwall contribution to the mixing loss ($\xi_{mixing,end}$) calculated. The Streamwise Momentum Deficit loss is then found by subtracting the SKE loss from equation (14):

$$\xi_{mom-mix} = \xi_{mixing,end} - \xi_{SKE} \qquad (15)$$

As shown in Figure 8 this component of loss rises approximately linearly with the Amplification Factor, and has relatively low sensitivity to the inlet boundary layer thickness compared to the SKE loss. For the low-turning design the streamwise momentum

deficit loss is small (~0.0015) and is approximately equal to the overall secondary-flow-induced loss for this design (Figure 4). For the high-turning design, the momentum deficit loss is slightly larger but represents a smaller fraction of the overall loss.

From the relative magnitude of each term in Figure 6 to Figure 8, it is clear that it is largely the Secondary Kinetic Energy (Figure 7) that determines the sensitivity to inlet conditions. The results also reveal a switch in mechanism for the secondary-flow-induced loss: low-turning designs are dominated by the mixing-out of Streamwise Momentum Deficits; while for higher-turning designs the SKE tends to dominate. An extreme example of this behaviour is a zero-turning duct with no blades, no secondary flow generation and thus only loss from the mixing of Streamwise Momentum Deficits.

5. MODELLING SECONDARY FLOW

Having demonstrated that SKE dominates the sensitivity of endwall loss to inlet conditions, the analysis now applies a theoretical model to highlight the underlying physical mechanisms.

5.1 Vorticity Amplification Theory

The prediction of secondary flows was studied intensely in the early years of turbomachinery research. "Classical" theories focused on the analytical prediction of secondary vorticity and velocity, as reviewed by Horlock and Lakshminarayana [16]. Assuming inviscid flow, these methods predict the exit streamwise vorticity by considering the convection and reorientation of the inlet boundary layer vorticity as it convects through the blade row. For incompressible flow, Hawthorne [17] used a vortex-filament analysis and applied Helmholtz's theorems, while Came and Marsh [18] presented an alternative approach based on Kelvin's Circulation theorem. Both approaches give the same expression for the distributed vorticity associated with the passage vortex and bulk secondary flow.

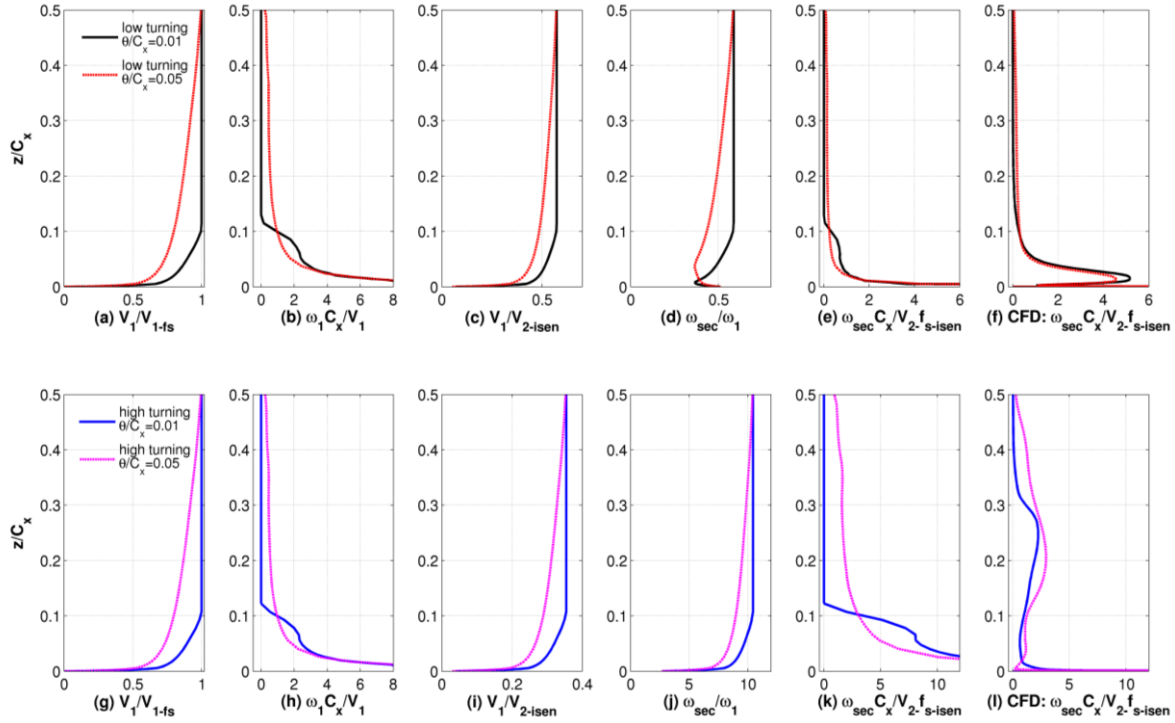

Figure 9: Vorticity Calculations for the low-turning (top row) and high-turning (bottom row) designs: (a, g): inlet velocity; (b, h): inlet vorticity; (c, i): isentropic velocity ratio; (d, j): vorticity ratio (eq. (16)); (e, k): calculated exit streamwise vorticity; (f, l): CFD streamwise vorticity at the trailing edge plane.

This paper applies the method of Marsh [4] who extended the circulation analysis to include compressibility. The method assumes that the flow through the blade row is parallel to the endwall, without streamtube contraction or twist. At each spanwise height the ratio of outlet-streamwise vorticity to the inlet-boundary layer vorticity is given by:

$$\frac{\omega_{sec}}{\omega_1} = M^* \left(\frac{V_1}{V_2}\right)\left[\frac{\Delta T^* C_x}{p\cos\alpha_2} + \frac{\left|\left(\frac{V_2}{V_1}\right)\sin\alpha_1 - \sin\alpha_2\right|}{\cos\alpha_2}\right] \qquad (16)$$

This equation has been applied to each case using the radial-averaged inlet conditions from the CFD calculations (total pressure, static pressure and flow angle) and area-averaged outlet pressure. Figure 9 illustrates the vorticity calculations for the low (a-f) and high (g-l) turning designs with two different inlet conditions.

Figure 9(a) and (g) show the normalised inlet velocity profiles; Figure 9(b) and (h) show the associated boundary layer vorticity. By definition the area-averaged inlet vorticity is independent of the boundary layer thickness. The thicker boundary layer has higher vorticity in the "outer" region of the span ($z/C_x > 0.1$); while thinner boundary layers have higher vorticity levels in the "inner" region ($z/C_x < 0.1$, only partially visible on this scale).

The terms in equation (16) are calculated at each height. The velocity ratio V_1/V_2 is assumed to be the isentropic velocity ratio V_1/V_{2-isen} at each height, presented in Figure 9(c) and (i). The transit time difference ΔT^* is assumed to scale with the local exit velocity, so that $\Delta T^* \sim 1/V_{2-isen}(z)$, which results in small variations up the span. The inlet and exit flow angles are taken as the midspan values. The resultant vorticity ratio ω_{sec}/ω_1 (equation (16)) is presented in Figure 9(d) and (j). This parameter varies slightly up the span and with boundary layer thickness, largely due to variation in the velocity ratio V_1/V_{2-isen}.

The calculated outlet streamwise vorticity is presented in Figure 9(e) and (k). For each design, the overall pattern of outlet vorticity largely follows that of the inlet vorticity. Thicker boundary layers cause higher levels of vorticity in the outer region ($z/C_x > 0.1$), while thinner boundary layers cause higher levels of vorticity close to the endwall, but the overall area-averaged vorticity changes only slightly. It will be demonstrated in section 5.2 that these changes in vorticity distribution impacts the resultant SKE significantly.

For comparison, Figure 9(f) and (l) present equivalent data from the trailing edge plane of the CFD calculations: streamwise vorticity of the same sign as the passage vortex has been mass-averaged in the pitchwise direction. For the low-turning design the model (Figure 9(e)) and CFD (Figure 9(f)) show reasonable agreement. As the boundary layer thickness is increased, the two plots show an increase in vorticity in the outer region ($z/C_x > 0.1$) and reduction in the inner region. Some differences are observed in the inner region, where the peak vorticity in the CFD is displaced from the endwall due to the effects of streamtube twist and viscous dissipation close to the wall. For the high-turning design, Figure 9(k) and (l) show larger differences. As θ/C_x is increased, the increase in vorticity in the outer region is similar for the two cases. However, the CFD results indicate significant streamtube twist and re-distribution of the vorticity towards midspan. Gregory-Smith et al. [9] made similar observations when comparing measured streamwise vorticity distributions to secondary flow theory. Nonetheless, the simple Marsh model captures the broad trends observed in the CFD. The analysis could be improved to include streamtube twist, but this increases the complexity significantly (e.g. [19]). Other limitations include the neglection of streamtube contraction, and the method does not explicitly account for the horseshoe vortex, e.g. for a zero-turning symmetric strut, equation (16) returns $\omega_{sec} = 0$.

5.2 Secondary Flow Velocities and SKE

The secondary velocities associated with the predicted vorticity field of the Marsh model are calculated via a streamfunction ψ (Squire and Winter [20]), such that:

$$W = \frac{d\psi}{dy_{norm}},\ V_{norm} = -\frac{d\psi}{dz} \qquad (17)$$

where V_{norm} and y_{norm} are the velocity and distance perpendicular to the primary flow (α_2-direction). A numerical solution is obtained for each case using the vorticity field ([21]):

$$\frac{\partial^2\psi}{\partial y_{norm}^2} + \frac{\partial^2\psi}{\partial z^2} = -\omega_{sec} \qquad (18)$$

It is worthwhile to highlight the importance of the definition of the primary flow direction. For the low-turning design, Figure 10(a) shows the Marsh model prediction of secondary flow streamlines with contours of SKE loss (equation (14)). Figure 10(b) shows the equivalent CFD data at the trailing edge plane, with the primary flow angle defined as the mass-averaged value $\overline{\alpha_2}$. The streamline patterns are very different, and SKE is high at the midspan due to the variation of flow angle across the pitch. In Figure 10(c) the primary flow is defined by the midspan flow angle at each pitchwise location, which automatically sets the SKE at midspan to be zero and allows a more appropriate comparison with the model. This definition of primary and secondary flow is therefore used throughout this paper.

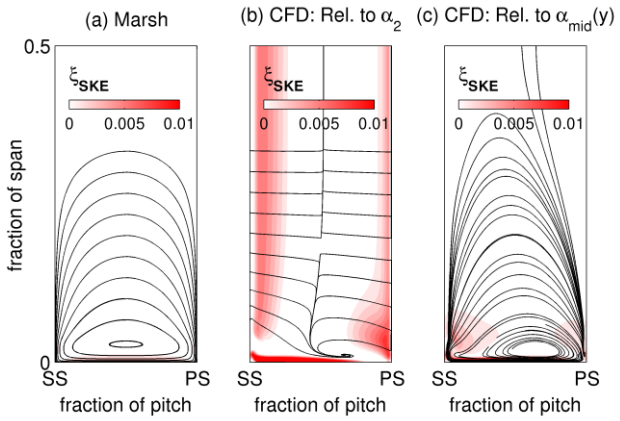

Figure 10: Secondary Flow Definitions for the low-turning design, $\theta/C_x = 0.01$; pitchwise direction is normal to the exit flow angle.

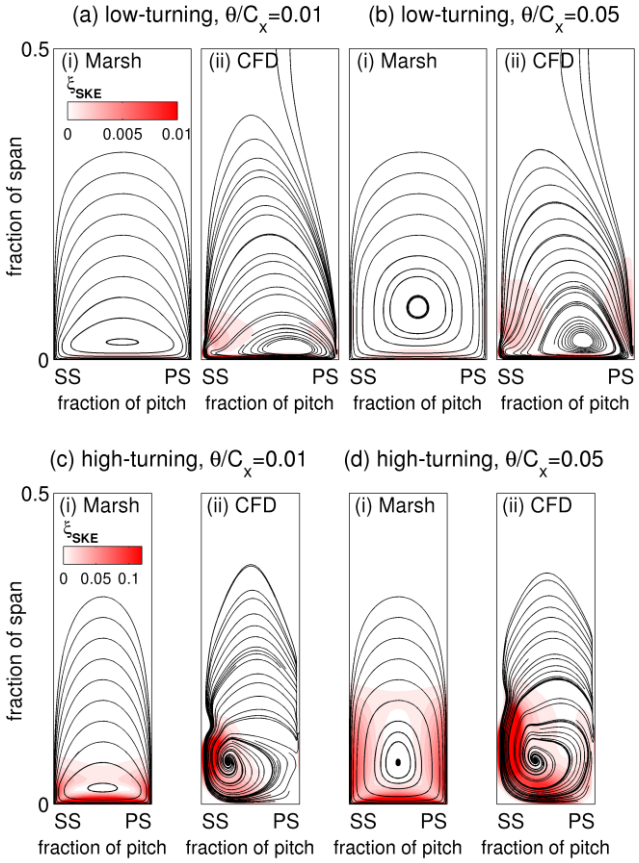

Figure 11: Secondary-Flow Streamlines and SKE: Marsh model and CFD results; pitchwise direction is normal to the exit flow angle.

Figure 11 compares the Marsh predictions to the CFD results for the low and high-turning cascades, with two inlet boundary layer thicknesses. The lack of streamtube twist in the model always leads to symmetric solutions. For the high-turning CFD results (Figure 11(c)(ii) and (d)(ii)) there is significant streamtube twist and asymmetry. In particular, the vortex core has moved towards the blade suction surface inducing high SKE in this region. Despite these differences the Marsh model does a reasonable job of capturing the overall pattern of the secondary flow and the size of the passage vortex. The order-of-magnitude increase in SKE between the low and high-turning designs is captured (note the different scales); the model also predicts the higher SKE for the thicker inlet boundary layer, in particular for the high-turning design (Figure 11(c) and (d)). The Marsh model highlights the importance of the *distribution* of secondary vorticity within the passage. As the boundary layer thickness increases, the average

vorticity level remains approximately constant but the vorticity becomes more dispersed within the passage (Figure 9 (e) and (k)). This dispersed vorticity field results in larger secondary flow structures with higher overall secondary kinetic energy.

For all of the cases studied, Figure 12 compares the SKE loss from the Marsh model with the CFD values extracted at the trailing edge plane. Reasonably good agreement is found for most designs. For the high-turning design the modelled values are higher but this likely reflects the increased dissipation of SKE within the blade passage for this design (Figure 6).

Figure 13 presents the SKE loss for the Marsh model plotted against the Amplification Factor, which is in close agreement to the CFD data in Figure 7. The trends in Figure 13 re-iterate the two factors determining SKE:

1. *The average value of secondary vorticity* $\overline{\omega_{sec}}$ is determined by the two-dimensional blade design, and is approximately independent of the inlet boundary layer thickness. For a fixed boundary layer thickness, the Secondary Kinetic Energy increases with $\overline{\omega_{sec}}^2 \propto AF_{Marsh}^2$ as one moves left-to-right in Figure 13 (i.e. from low-turning to high-turning designs).
2. *The distribution of vorticity within the passage*, which is determined by the inlet boundary layer. Thin inlet boundary layers tend to produce secondary flows structures that remain close to the endwall (e.g. Figure 11(c)). Thickening the inlet boundary layer displaces vorticity away from the endwall, tending to generate larger secondary flow structures (e.g. Figure 11(d)). Such larger vortex structures tend to have higher associated SKE (e.g. Clark et al. [22]), leading to an increase in loss.

For designs with high AF_{Marsh} and thus high average vorticity, significant variation in endwall loss is introduced by the vorticity distribution effects.

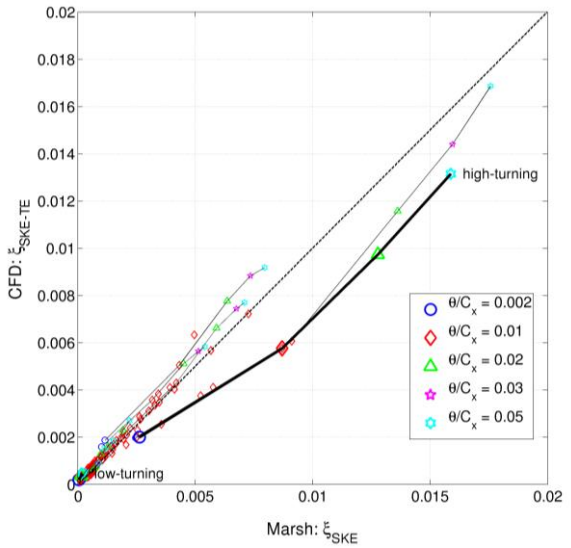

Figure 12: Comparison of Marsh-predicted SKE loss coefficient with the CFD calculations.

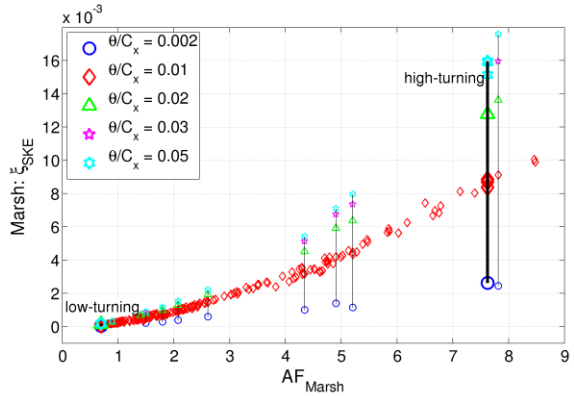

Figure 13: SKE loss for the Marsh calculations, analogous to the CFD data in Figure 7.

6. CONCLUSIONS

- The sensitivity of endwall loss to inlet conditions is design-dependent, and is largely driven by the component of loss associated with the secondary flow and associated mixing processes.

- The Secondary-Flow-Induced loss can be characterised by an Amplification Factor (AF_{Marsh}), which is a measure of the average outlet secondary vorticity. Blade designs with higher Amplification Factor (e.g. high-turning designs) tend to have higher loss and are more sensitive to the inlet boundary layer thickness.
- The sensitivity is primarily driven by the dissipation of Secondary Kinetic Energy (SKE). To a first order, the SKE generated by a turbine cascade is governed by the average level of streamwise vorticity ($\propto AF_{Marsh}$) and its distribution in the passage. The distribution of vorticity is strongly influenced by the inlet boundary layer thickness: thicker inlet boundary layers cause the secondary vorticity to be more dispersed within the passage, resulting in larger secondary flow structures and higher SKE.
- Designs with low Amplification Factor (AF_{Marsh}) have relatively low SKE and therefore exhibit only weak sensitivity to inlet conditions.
- The variations in SKE can be captured using a simple model based on the inviscid vorticity calculation of Marsh [2] and the streamfunction approach of Squire and Winter [20]. A similar approach could be used to perform sensitivity assessments in the preliminary stage of design, and could be readily extended to engine-realistic boundary conditions.

7. NOMENCLATURE

Symbols

A	Area
AF_{Marsh}	Vorticity Amplification Factor (equation (5))
AR	Aspect Ratio $= h/C_x$
C_D	Dissipation Coefficient
c_p	Specific Heat Capacity (isobaric)
C_p	Pressure Coefficient $= (P_{01} - P)/(P_{01} - P_2)$
C_{p-TE}	Pressure Coefficient $= (P_{01} - P)/(P_{01} - P_{SS-TE})$
C_x	Axial Chord
h	Specific Enthalpy
H	Span
$\dot{m}$	Mass flow rate
M	Mach number
p	Pitch
P, P_0	Static and Total Pressure
Re_{C_x}	Axial Chord Reynolds number $= V_2 C_x/v$
s	Specific Entropy
S	Distance along Surface
t	Trailing Edge Thickness
T	Temperature
T^*	Non-Dimensional Surface Transit Time
V	Velocity
x	Axial Distance
y	Pitchwise Distance
Y_p	Total Pressure Loss Coefficient
z	Spanwise Distance
Z_w	Zweifel Lift Coefficient
α	Flow Angle
γ	Specific Heat Ratio
δ^*	Inlet Boundary Layer Displacement Thickness
θ	Inlet Boundary Layer Momentum Thickness
v	Kinematic Viscosity
ξ	Entropy Loss Coefficient
ρ	Density
ω	Vorticity

Subscripts and Abbreviations

0	Stagnation
1, 2	Row Inlet and Outlet
CD	Background Endwall Boundary Layer Dissipation
DF	Diffusion Factor $= \sqrt{(C_{p-TE}(peak) - 1)}$
fs	Boundary layer edge
$isen$	Isentropic

LE Leading Edge
mid Midspan (Profile)
mix Mixed-Out (Constant-Area)
mom Streamwise Momentum Mixing Loss
$norm$ Normal to Primary-Flow and Spanwise directions
PS Pressure Surface
PSL Peak Suction Location (fraction of surface length)
sec-flow Secondary-Flow-Induced Loss
SKE Secondary Kinetic Energy
SS Suction Surface
TE Trailing Edge

REFERENCES

[1] Sieverding, C.H., 1985, "Recent Progress in the Understanding of Basic Aspects of Secondary Flows in Turbine Blade Passages", ASME. *J. Eng. Gas Turbines Power.* 1985;107(2) pp. 248-257

[2] Langston, L.S., 2001, "Secondary flows in axial turbines—a review" *Annals of the New York Academy of Sciences* 934.1 (2001) pp. 11-26

[3] Coull, J.D., 2017, "Endwall Loss in Turbine Cascades", ASME. *J. Turbomach.* Vol. 139(8) pp. 081004

[4] Marsh, H., 1976, "Secondary Flow in Cascades – The Effect of Compressibility", *Aeronautical Research Council R&M* No. 3778

[5] Denton, J.D., 1993, "Loss Mechanisms in Turbomachines" ASME. *J. Turbomach.,* Vol. 115(4), pp. 621-656

[6] Denton, J.D. and Pullan, G.P., 2012, "A Numerical Investigation into the Sources of Endwall Loss in Axial Flow Turbines", ASME paper GT2012-69173

[7] Halstead, D.E., 1996, "Boundary Layer Development in Multi-Stage Low Pressure Turbines" PhD Thesis, Iowa State University

[8] Sharma O.P., and Butler, T.L., 1986, "Predictions of Endwall Losses and Secondary Flows in Axial Flow Turbine Cascades." ASME paper 86-GT-228

[9] Gregory-Smith, D.G., Graves, C.P., and Walsh, J.A., 1988, "Growth of Secondary Losses and Vorticity in an Axial Turbine Cascade", ASME. *J. Turbomach.,* Vol. 110(1), pp. 1-8

[10] Hodson, H.P. and Dominy, R.G., 1987, "The Off-Design Performance of a Low-Pressure Turbine Cascade" ASME. *J. Turbomach.,* Vol. 109(2), pp. 201-209

[11] de la Rosa Blanco, E.R., Hodson, H.P., Vazquez, R. and Torre, D., 2003, "Influence of the State of the Inlet Endwall Boundary Layer on the Interaction Between Pressure Surface Separation and Endwall Flows". *Proceedings of the Institution of Mechanical Engineers, Part A: Journal of Power and Energy*, *217*(4), pp.433-441.",

[12] Shahpar, S., and Lapworth, L., 2003, "PADRAM: Parametric Design and Rapid Meshing System for Turbomachinery Optimisation", ASME Paper GT2003-38698

[13] Moinier, P., and Giles, M.B., 1998, "Preconditioned Euler and Navier-Stokes Calculations on Unstructured Grids", 6th ICFD Conference on Numerical Methods for Fluid Dynamics

[14] Halstead, D.E., 1996, "Boundary Layer Development in Multi-Stage Low Pressure Turbines" PhD Thesis, Iowa State University

[15] Coull, J.D., Clark, C.J. and Vazquez, R., 2017, "Turbine Cascade Endwall Loss: Inlet Conditions and Vorticity Amplficiation" Global Power and Propulsion Forum, Zurich, Jan 2017 GPPF-2017-72

[16] Horlock, J.H. and Lakshminarayana, B., 1973. Secondary flows: theory, experiment, and application in turbomachinery aerodynamics. *Annual Review of Fluid Mechanics*, *5*(1), pp.247-280.

[17] Hawthorne, W.R., 1955, "Rotational Flow Through Cascades: Part 1: The Components of Vorticity", *Quart. Journ. Mech. and Applied Math.,* Vol 8(3)

[18] Came, P.M. and Marsh, H., 1974. "Secondary flow in cascades: two simple derivations for the components of vorticity". *Journal of Mechanical Engineering Science*, *16*(6), pp.391-401

[19] Okan, M.B. and Gregory-Smith, D.G., 1992, "A simple method for estimating secondary losses in turbines at the preliminary design stage", ASME paper 92-GT-294

[20] Squire, H.B. and Winter, K.G., 1951, "The Secondary Flow in a Cascade of Airfoils in a Nonuniform Stream", *Journal of the Aeronautical Sciences,* April 1951

[21] Glynn, D.R. and Marsh, H., 1980. Secondary flow in annular cascades. *International Journal of Heat and Fluid Flow*, *2*(1), pp.29-33

[22] Clark, C.J., Pullan, G., Curtis, E. and Geonaga, F., 2016, "Secondary Flow Control in Low Aspect Ratio Vanes using Splitters", ASME paper GT2016-56625